Ahmed Aseem, Ching Tai Ng

Debonding detection in rebar-reinforced concrete structures using second harmonic generation of longitudinal guided wave

NDT & E International, 2021; 122:102496-1-102496-12

Final publication at: http://dx.doi.org/10.1016/j.ndteint.2021.102496

Journal article:

Ahmed Aseem , Ching Tai Ng. (2021). Debonding detection in rebar-reinforced concrete structures using second harmonic generation of longitudinal guided wave. NDT & E International, 122:102496.

Debonding Detection in Rebar-reinforced Concrete Structures Using Second Harmonic Generation of Longitudinal Guided Wave

Ahmed Aseem[1] and Ching Tai Ng[*1]

[1] School of Civil, Environmental & Mining Engineering, The University of Adelaide

Abstract

Nonlinear features of ultrasonic guided waves (GWs) is studied for debonding detection and location estimation in rebar reinforced concrete structure. The study shows that the presence of debonding between steel rebar and concrete surface produces breathing phenomenon causing contact acoustic nonlinearity (CAN), which generates second harmonics. Time-frequency analysis is used to estimate the location of debonding in this study. At a particular frequency, embedded rebar has much greater number of wave modes in bare rebar. To avoid unnecessary complexity, only longitudinal GW modes for bare and embedded rebar are excited and received to detect and locate debonding. To precisely determine the wave mode at excited frequency and frequency of second harmonics, frequency-wavenumber analysis is performed using 2D-Fast Fourier Transform of time-space data. Three-dimensional explicit finite element simulations are performed for various case studies and the model is validated by experimentally measured data. The results of this study show that the proposed method is practically viable and beneficial for debonding detection and location estimation in reinforced concrete structures.

[*] Corresponding author: alex.ng@adelaide.edu.au

Keywords: Debonding; Nonlinear guided wave; Reinforced concrete structure; Second harmonic; Contact acoustic nonlinearity

1 Introduction

Civil engineering structures made by reinforced concrete are vital part of our infrastructure. These structures are subjected to environmental and external loading, along with corrosion and fatigue, which can lead to damage and degradation. The integrity of these structures cannot be neglected. The bonding between steel rebar and concrete develops required strength in reinforced concrete structures. Corrosion and debonding can significantly reduce the ultimate strength and serviceable life of the reinforced concrete structure [1]. Different Structural Health Monitoring (SHM) techniques have been developed by researchers to assess the integrity of various structures. Linear and nonlinear features of ultrasonic guided waves (GWs) have been proven to be reliable in damage detection. The linear features of ultrasonic GWs have been found to be sensitive to gross defects in structures, such as holes, notches and open cracks etc [2]. The nonlinear features have been recognised to be more sensitive to material nonlinearities, fatigue cracks, fatigue and material degradation [3, 4].

1.1 Linear features of ultrasonic guided waves

Linear features of ultrasonic GWs, for example, wave amplitude, velocity, energy and time-of-flight (ToF) were used by many researchers for detecting damage in reinforced concrete structures and composites. In the literature, GWs have been widely recognized as one of the promising techniques for damage detection in reinforced concrete structures. The surface cracks in reinforced concrete can be detected using linear features [5, 6]. Steel rebar damage in concrete was studied by Lu *et al*. and Mustapha *et al*. [7, 8] using linear features of ultrasonic GWs and they proposed a time reversal method to detect the damage. Similarly, GWs have also been used to monitor reinforced concrete beam subjected to damage using embedded and surface bonded piezo electric transducers [9]. Zhu *et al*. [10] demonstrated the use of linear features of GWs in detecting debonding between steel and concrete at various locations in reinforced concrete structures. Wu and Chang [11, 12] experimentally observed the linear feature of GWs for steel debonding in concrete subjected to loading. The sensitivity of energy distribution of GWs for debonding detection using wavelet technique were studied for reinforced concrete [13]. Mohseni and Ng studied the scattering of linear GWs at surface debonding in fibre reinforced polymer (FRP) retrofitted concrete structure [14].

Ultrasonic GWs are also capable of monitoring accelerated corrosion at steel bar in reinforced concrete [15-19]. Recently, Zima and Kedra [20, 21] used one of the linear features of GWs, time-of-flight of different GW modes, for debonding size estimation in reinforced concrete beams. They used variation of group velocities in debonded region to detect damage. The effect of multiple debondings was also studied but the linear features were unable to detect the location of debonding. The aforementioned damage detection methods used the variation in voltage, velocity, time-of-flight, amplitude and energy of GWs to detect the damage. However, damage detection methods require baseline data as the damage detection is achieved by comparing the measured data from intact structures and the structures with the damage. The variation of environmental conditions, such as temperature and external loading, can make the baseline subtraction fail in extracting the damage information from the measured data. In the literature, nonlinear features of GWs have demonstrated their feasibility for damage detection without using the baseline data.

1.2 Nonlinear features of guided waves

When ultrasonic waves interact with material nonlinearity and/or contact type of damages, the fundamental wave energy converts into higher harmonics, which is one of the nonlinear features of GWs. In the literature, nonlinear features of GWs have been proven to be promising for damage identification and quantification. Soleimanpour and Ng [22] used second harmonic generation of GWs to detect and locate delamination in laminated composite beams. Mohseni and Ng demonstrated that the higher harmonic generation in FRP-retrofitted concrete structures can be used to detect debonding [23]. Chen *et al.* showed that the presence of surface cracks in bending concrete also generate second harmonics due to the breathing effect [24]. But these studies were limited to detect debonding between FRP and concrete, or crack in reinforced concrete structures using second harmonics of GWs.

The presence of debonding between steel rebar and concrete can significantly reduce the stiffness of the reinforced concrete structures. In the literature, majority of the studies only used linear features of GWs to detect debonding and they require baseline data to extract the linear features, which are not sensitive to debonding. It has been recognized that second harmonic is potential to detect damage without using the baseline data. Therefore, an insight into the nonlinear features, such as second harmonic, is required to develop methods for debonding detection.

Second harmonics can be produced due to the presence of material nonlinearity and imperfections. When wave interacts with weak material nonlinearity, higher order harmonics are generated and they have been studied by many researchers [25-29]. The presence of imperfections in materials, such as micro cracks, holes, discontinuities and delamination produce contact surfaces within material, can lead to the second harmonic generation [30]. This phenomenon is known as contact acoustic nonlinearity (CAN). Solodov *et al*. have described the phenomenon of generation of higher harmonics due to clapping interfaces in detail [31]. It enables fundamental wave mode generating second harmonics while interacting with defects. These kinds of studies have been carried out to detect cracks, fatigue and other defects in plate-like structures [24, 32, 33]. Klepka *et al.*

studied nonlinear vibro-acoustic wave interaction mechanism to detect contact damage in aluminium plate [34]. Guan *et al*. [35] detected fatigue cracks in pipe using nonlinear GWs. But the nonlinear features of GWs have not been widely studied for contact type damages for embedded rebar in concrete. The nonlinear features are baseline free techniques for damage detection and have therefore advantage over linear features. For embedded structures such as rebar in concrete, no significant research has been reported to detect damage using nonlinear features. The paper also studies the time-frequency analysis, which is used for debonding location estimation. Although linear techniques are available for damage estimation in embedded rebar but the nonlinear baseline free technique is proposed to be a useful method in civil engineering applications. This paper focuses on the use of linear and nonlinear features, i.e. second harmonic of longitudinal GWs, to detect the debonding between in rebar and concrete. The exposed ends of embedded rebar are considered for excitation and receiving to understand wave propagation phenomenon for the fundamental study as mentioned in this paper.

This paper is organized as follows. The proposed methodology is presented in Section 2. Numerical and experimental investigations are described in Sections 3 and 4, respectively. The results are then discussed and used to elaborate the use of nonlinear features in detecting and locating debonding between steel rebar and concrete in Section 5.

2 Proposed Methodology

For reinforced concrete structures with debonding between rebar and concrete, there are two types of nonlinearity can generate second harmonics. They are weakly material nonlinearity and contact nonlinearity, which is caused by the debonding between steel rebar and concrete. The study focuses on CAN, which has proven to have much larger magnitude of second harmonic as compared to that generated by material nonlinearity. This makes it easier to be used for damage detection [36]. The debonding (contact damage) can be detected and quantified using a ratio of second harmonic amplitude (A_2) to fundamental frequency amplitude (A_1), i.e. $\beta = A_2/A_1$, where β is nonlinear acoustic parameter for contact type of damage.

2.1 Debonding detection using second harmonics

When GW propagates in embedded rebar, various wave modes are generated. Due to the presence of surrounding concrete, the energy of GW is leaked from rebar to concrete as shown in Figure 1. However, the energy will not be leaked into concrete if the phase velocity of propagating wave in rebar is less than the bulk shear and longitudinal velocities of the concrete. There are two cases of wave energy leakage, (a) when phase velocity is greater than the bulk shear wave and less than the bulk longitudinal wave velocity of concrete, only shear wave is leaked from rebar into concrete; (b) when phase velocity is greater than both the bulk shear and longitudinal wave velocity of concrete, both bulk and shear wave energy is leaked from rebar into concrete [37]. Considering the phase velocity of steel rebar is greater than either shear or longitudinal wave of concrete, the energy is likely to be leaked into concrete. However, the propagation of GW in embedded rebar produces multiple wave modes and this will be discussed later. The leaked energy will not provide enough information for debonding detection. The interaction of wave propagating in embedded rebar with debonding is the main focus of this study. The presence of debonding at rebar in concrete creates discontinuity between rebar and concrete surface and affects the GW propagation. The discontinuity behaves as contact surface and second harmonics are generated due to the CAN phenomenon as shown in Figure 1. When a GW with tension and compression components passes through a debonding region, the contact surfaces of rebar and concrete open due to tensile components of the wave and close due to compression components. When GW interact at the debonding, the opening and closing of contact surfaces generate second harmonics.

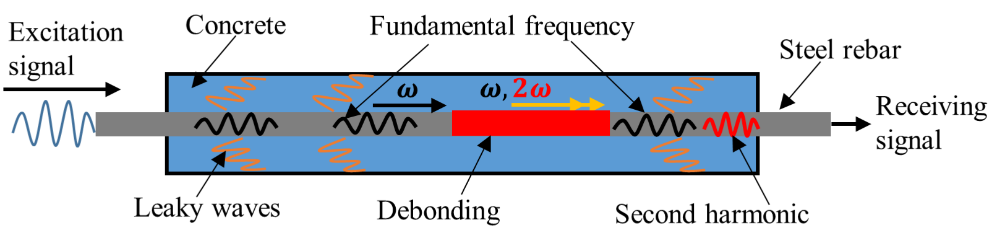

Figure 1. Generation of second harmonics at debonding between rebar and concrete

After the GW passed through the debonding, the propagating GW consists of fundamental and second harmonics. The presence of second harmonic provides valuable information for debonding detection. The debonding of varying sizes can be quantified using relative nonlinear acoustic parameter β discussed earlier of this section. Based on the generation of second harmonic, damages can be quantified, and therefore, serves as an important indicator for SHM.

2.2 Guided wave modes in bare rebar and rebar embedded in concrete

For debonding detection in steel rebar reinforced concrete, the GW propagation in bare rebar and embedded rebar is investigated in this section. It is necessary to understand different GW modes in bare steel rebar and embedded rebar as shown in Figure 1. Three GW modes can exist in circular waveguide, they are longitudinal L(0,n), torsional T(0,n) and flexural F(1,n) wave mode, where n represents the mode order, while 0 and 1 are for symmetric and asymmetric wave fields, respectively. For rebar embedded in concrete, the number of flexural GW modes is greater than longitudinal and torsional modes. Moreover, torsional GW modes have greater attenuation in embedded rebar than flexural and longitudinal modes. For simplicity in analysis, only longitudinal GW modes are excited and measured. The group velocity dispersion curve of longitudinal GW modes for 10mm radius bare circular steel rebar is calculated using DISPERSE software[37]. GW modes propagating in structures embedded in concrete have greater number of wave modes. For 10mm radius steel bar embedded in concrete having outer diameter of 100mm, the first 13 longitudinal wave modes were calculated using DISPERSE and the results are shown as L(0,1) – L(0,13) in Figure 2. The circular cross-section of concrete was chosen because of simplicity in calculating the dispersion curves in DISPERSE. The properties of the steel and concrete are listed in Table 1.

[Table 1. Material properties of steel and concrete]

Material	Density (kg/m^3)	Elastic Modulus (GPa)	Poisson's ratio
Steel	7880	207	0.33
Concrete	2289	32.5	0.14

There are only two longitudinal GW modes existed in bare rebar shown as $L(0,1)_b$ and $L(0,2)_b$, while embedded rebar in concrete has 13 longitudinal GW modes within the frequency range of 0-200 kHz as shown in Figure 2. The subscript b means the results are for bare rebar. The fastest wave mode in bare rebar is $L(0,1)_b$, while the second order longitudinal wave mode $L(0,2)_b$ appears after 180 kHz. The group velocities of embedded rebar wave modes L(0,1) – L(0,7) have smaller value than that of $L(0,1)_b$ for frequency less than 132 kHz.

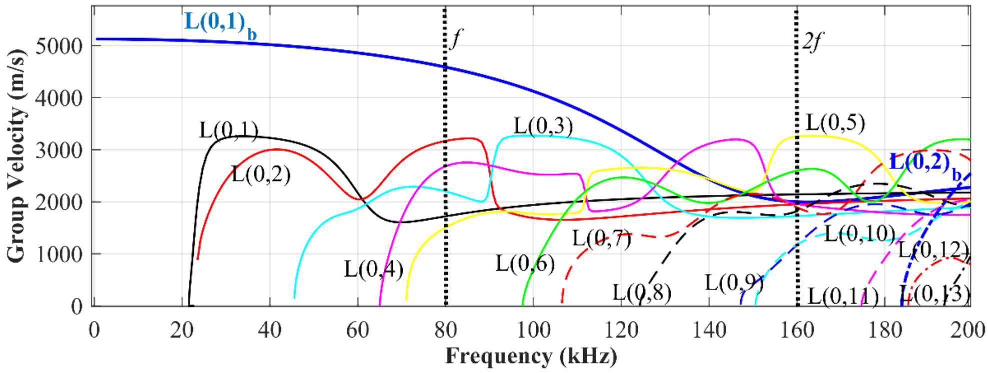

Figure 2. Group velocity dispersion curve for bare steel rebar and steel rebar embedded in concrete

2.3 Estimation of debonding location using second harmonic

The use of linear features for damage detection in rebar reinforced concrete requires baseline data from undamaged specimen[38]. Nonlinear feature, such as second harmonic, is proposed in this study to overcome the shortcomings of linear features. The behaviour of GWs in bare rebar and rebar embedded in concrete is different in terms of various mode generation. A schematic diagram of reinforced concrete beam specimen is shown in Figure 3. When wave is excited at the end of bare steel rebar, GW modes propagate. Upon entrance into intact concrete, various wave modes are generated, which can be observed in the dispersion curve of rebar embedded in concrete. These wave modes at fundamental frequency (f) travel at different wave speeds with few wave modes arriving earlier than the others. When these wave modes interact with debonding (contact nonlinearity), second harmonics are produced. The group velocity of second harmonic wave modes is different to first harmonic and they have different wavelengths at second harmonics ($2f$). Due to the change in velocity, the first harmonic wave arrives the other end of the rebar at a time different to the second harmonic .

The presence of arrival time delay in first and second harmonics provides valuable information to determine the debonding location. The second harmonics are not produced instantly at the interaction of respective fundamental wave mode with contact damage. There is time delay in generation of second harmonics at debonding when the wave interacting with contact surfaces. It needs to be taken into account for accurate estimation of the debonding location. This will be further discussed in Section 5. After passing from concrete into steel at receiving end, the wave travel at group velocity of wave mode in bare steel bar at respective frequency.

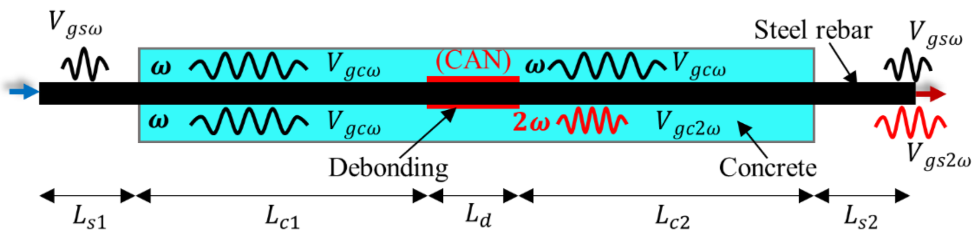

Figure 3. Schematics for fundamental and second harmonic wave propagation in reinforced concrete

The arrival time of first and second harmonics using parameters in Figure 3 can be calculated

$$T_{\omega} = \frac{L_{s1}}{V_{gs\omega}} + \frac{L_{s2}}{V_{gs\omega}} + \frac{L_{c1}}{V_{gc\omega}} + \frac{L_{c2}}{V_{gc\omega}} + \frac{L_d}{V_{gc\omega}} \tag{1}$$

$$T_{2\omega} = \frac{L_{s1}}{V_{gs\omega}} + \frac{L_{s2}}{V_{gs2\omega}} + \frac{L_{c1}}{V_{gc\omega}} + \frac{L_{c2}}{V_{gc2\omega}} + \frac{L_d}{V_{gc2\omega}} + t_d \tag{2}$$

where

T_{ω} = arrival time of first harmonics

$T_{2\omega}$ = arrival time of second harmonics

L_{s1} = length of bare steel at excitation end

L_{s2} = length of bare steel at receiving end

L_{d} = length of debonding

L_{c1} = length of embedded steel from excitation end till debonding

L_{c2} = length of embedded steel from debonding till receiving end

$V_{gs\omega}$ = group velocity of first harmonic in bare steel

$V_{gs2\omega}$ = group velocity of second harmonic in bare steel

$V_{gc\omega}$ = group velocity of first harmonic for embedded steel in concrete

$V_{gc2\omega}$ = group velocity of second harmonic for embedded steel in concrete

t_{d} = time delay in generation of second harmonic at debonding

Δt = difference in time of arrival of first harmonics T_{ω} and second harmonics $T_{2\omega}$

By knowing Δt as delay in second harmonics $(T_{2\omega} - T_{\omega})$, location of debonding as d_l can be found using equation (4) and (5) as

$$d_l = \frac{(\Delta t - t_d - c)\left(V_{gc2\omega}.V_{gc\omega}\right)}{V_{gc\omega} - V_{gc2\omega}} \qquad (3)$$

where $d_l = L_{c2} + L_d$ and c = $\frac{L_{s2}}{V_{gs2\omega}}$ - $\frac{L_{s2}}{V_{gs\omega}}$ is treated as time difference between first and second harmonics waves in bare steel bar at receiving end. The location of debonding estimated using equation (3) can be used to identify the debonding region. The effect of varying debonding length at different locations in debonding location estimation is studied using numerical and experimental analysis.

3 Finite Element Simulations

3.1 Finite element model of plain rebar and effect of ribs

The pattern on the surface of the ribbed steel rebar provides better bonding and slip resistance with concrete surface. The maximum bond stress of ribbed rebar is 2-3 times greater than that of plain rebar[39]. It is, therefore, important to observe the propagation of GWs in plain and ribbed rebar. The ribbed and plain rebar are modelled in Abaqus/Explicit. The plain rebar is modelled as circular cross-section with 20mm diameter while the ribbed rebar is modelled using spiral solid as ribs on the plain rebar. Typical dimensions of ribbed rebar are selected for the ribs on plain rebar in the model. The 20mm diameter of plain rebar is reduced to 19mm diameter with circular cross-section of spiral being 1mm in radius. The spiral is given 69 revolutions throughout 700mm length of plain rebar with10mm spacing between the ribs. With one complete circular revolution as 360°, total 24,840° of revolution are applied to spiral rib. The inner diameter of hollow spiral with 1mm thickness is the same as outside diameter of plain rebar. This allows them to be bonded together perfectly. Using tie constraints, the spiral ribs are perfectly bonded to the plain rebar to form the ribbed rebar as shown in Figure 4.

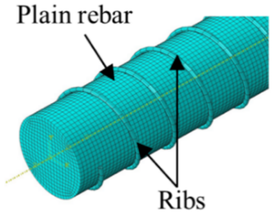

Figure 4. Meshing of ribbed rebar in ABAQUS

The Hann-windowed 8-cycle sinusoidal tone burst signal with central frequency of 80kHz was used as excitation pulse. At this frequency, the longitudinal wave mode $L(0,1)_b$ is well separated from higher order modes. Excitation signal was applied as the pressure to the cross-section of at the bar end. The hexagonal mesh type of 1mm size was chosen type for meeting quality meshing and this gives $L_e = \frac{\lambda}{20}$, where λ is the wavelength and L_e is the mesh size[40]. The finite element (FE) was chosen as C3D8R with three-dimensional (3D) stress and 8-noded solid element with reduced integration. The duration of the simulation is 0.7ms. The longitudinal GWs received at the other end of the plain and ribbed rebar were obtained by calculating the displacement in the direction of pressure applied. The obtained signals are shown in Figure 5. The signals received at the end of the plain and ribbed rebar are similar. The ribbed pattern on plain rebar does not have any significant effect on the GW propagation property. The wavelength of the excited pulse is 55mm, which is much larger than the rib spacing (10mm) on ribbed rebar. Therefore, the longitudinal GWs do not interact with ribs and generate other wave modes or reflection. In view of this, the plain rebar was used for debonding study in reinforced concrete due to ease of FE modelling, geometrical and practical considerations.

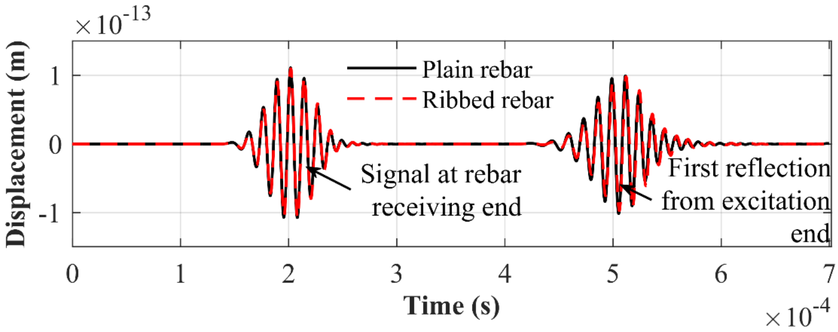

Figure 5. Comparison of L(0,1)b wave mode propagation in plain and ribbed rebar

The group velocity of the wave propagation can be calculated using $V_G = \frac{\Delta d}{\Delta t}$, where Δd and Δt are the distance and time difference between two measurement points of propagating wave, respectively. The group velocities of $L(0,1)_b$ at various frequencies calculated using FE model are plotted against theoretical dispersion curve, which were also validated through experimental study in Section 4. For the rebar embedded in concrete, various longitudinal GW modes were observed at a single frequency, which makes it complicated to separate the wave modes and calculate the group velocities. Considering this complexity, the group velocity dispersion was only validated for bare rebar.

3.2 Finite element model of reinforced concrete beam

A reinforced concrete beam with cross-section of 100mm×100mm and length of 700mm was selected for the study. The reinforcing rebar has 10mm radius with total length of 900mm and similar properties as listed in Table 1. The reinforcing rebar is extruding 100mm outside from each end of the beam for the ease of installation, wave excitation and measurement. A schematic diagram of the specimen is shown in Figure 6.

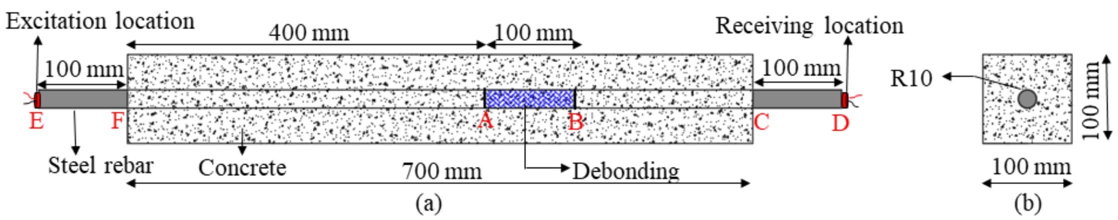

Figure 6. Reinforced concrete beam specimen (a) longitudinal view (b) cross-section

A 3D explicit FE method was used to study the generation and propagation of longitudinal GW in reinforced concrete beam as shown in Figure 7. The model is developed in Abaqus/CAE and is solved using Abaqus/Explicit. In reinforced concrete beam, the steel used for bare rebar FE model is restrained by increasing its length to 900 mm. For developing a reinforced concrete beam model, the steel rebar and rectangular concrete cross-section having 20mm Ø hole in centre is perfectly bonded together using tie constraints on the concrete and steel interfacial surfaces. A Hann-windowed 8-cycle tone burst signal at central frequency of 80 kHz is used as excitation signal from one end of extruding rebar by applying pressure on the surface of rebar at Point E. The mesh size for steel and concrete is 1mm as $L_e = \frac{\lambda}{20}$ [40]. The element for meshing is set to be three-dimensional eight-noded (C3D8R) having sweep hexagonal mesh type. For understanding the propagation of longitudinal GWs through the reinforced concrete beam, the displacement in the direction of rebar is measured at Point D. Initially, two reinforced concrete beam models with and without debonding are considered.

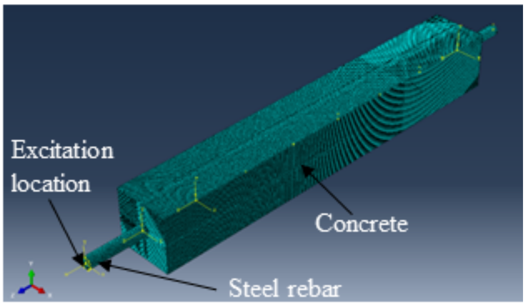

Figure 7. 3D view of the finite element model for reinforced concrete beam

To create the debonding between the rebar and concrete, the tie constraint between steel rebar and concrete surface is removed for the length of the debonding. To model the CAN effect for debonding, the circumferential surface of rebar for the debonding length was made to be clapped with concrete surface to generate second harmonic due to breathing effect. The simulation of the surface–surface contact interaction with frictionless surface was solved using penalty contact method. The perfectly bonded model is referred as Case N0, while the debonded specimen with debonding length of 100mm from region A-B shown in Figure 6 is referred as Case N1. The time-domain signal for cases N0 and N1 are shown in Figure 8, which are longitudinal GW modes with the estimated of arrival time using the group velocity dispersion curves as shown in Figure 2.

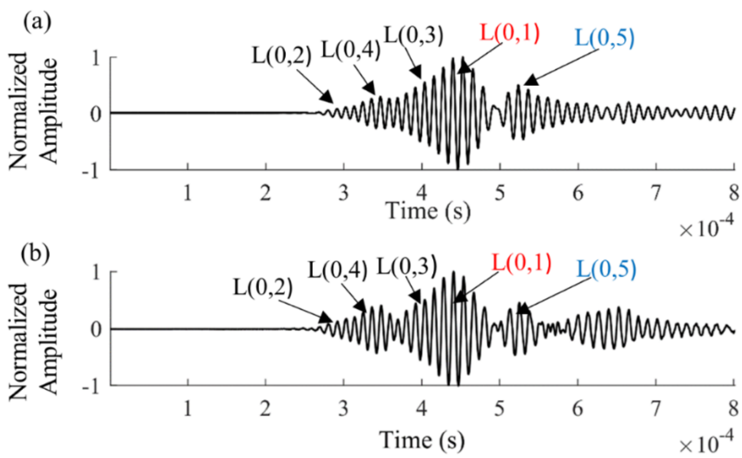

Figure 8. Time domain signal for numerical model (a) Case N0 without debonding (b) Case N1 with debonding

It is clearly represented that the L(0,1) wave mode arrives later than other higher order wave modes at the measurement location. The location of longitudinal wave modes i.e. L(0,1 – L0,5) on time domain signal is defined based on the group velocity dispersion curve for longitudinal wave. The higher order longitudinal wave modes, i.e. L(0,2), L(0,3) & L(0,4), arrive before L(0,1). The wave mode L(0,5) has group velocity slower than L(0,1) and it arrives after the L(0,1) wave. The variation in linear feature as time of arrival of various GW modes in debonded specimen requires baseline measurements from fully bonded specimen[7, 8]. Therefore, the time domain signal for debonded beam model alone does not provide significant information for the damage identification. The nonlinear features of second harmonics needs to be analysed for debonding detection and location estimation.

The simulation for representing behaviour of longitudinal GWs with debonding in rebar reinforced concrete is performed in shorter beam model to reduce the computation cost. For simulation purpose, the reinforced concrete beam specimen is reduced to 500mm in total length with 100mm length of plain rebar extruding out from each end leaving 300mm of embedded rebar in concrete. The cross-section of concrete and steel rebar is retained as same as in Figure 6(b) with similar material properties. The debonding length is chosen to be 100mm at the center embedded rebar in concrete. The numerical simulation for debonded specimen clearly represents the CAN effect at the location of debonding as shown in Figure 9. At the location of perfect bonding, the steel and concrete interfaces have compression and tension motion of GWs together, while the debonded region represents the opening and closure of debonded surface due to the breathing effect. The generation of secondary GW modes is studied using frequency analysis of time domain data after the discussion and comparison with experimental data in Section 4.

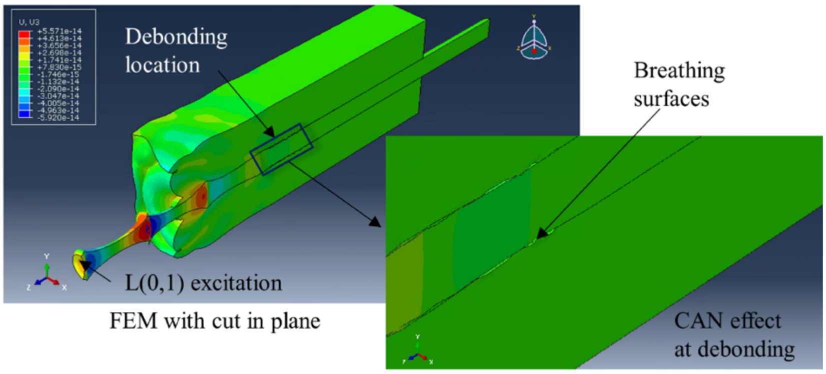

Figure 9. Numerical simulation representing CAN for debonding between steel rebar and concrete interface

4 Experimental Verification

In experimental study, the investigation for presence of debonding is carried out for the reinforced concrete beam specimen. As observed in time domain signal obtained from the FE model of specimen with the debonding, the information about presence of debonding is not obvious. Therefore, the time-frequency analysis is used to analyse the signal obtained from debonded and fully bonded reinforced concrete beam specimens. The experimentally measured time domain signals for bare and embedded plain rebar in concrete are compared with FE models.

4.1 Longitudinal guided wave in plain rebar

The propagation of longitudinal GW in plain rebar is compared with FE model described in 3.1. The plain steel rebar of 450mm in length and 20mm diameter is selected and has the same properties as those used in the numerical study for plain rebar. The longitudinal GW in steel rebar is actuated and received using 2mm thick and 10mm diameter circular piezoceramic transducers, which were attached to the centre of the cross-section located at the ends of the plain rebar as shown in Figure 10(a). The attached circular transducer at excitation location applies pressure to surface of rebar end and this is modelled in the numerical simulations. The signal is generated using National Instrument (NI) PXIe-1073, which has arbitrary waveform generator NI PXI-5412 and measured using signal digitizer NI PXI-5105. The NI system was connected to computer to generate and record the data. The same system setup was used for study in reinforced concrete beam specimen. A similar signal, which is a 8-cycle 80kHz sinusoidal tone burst modulated by Hann-windowed, was used in numerical case study and it was excited at the end of the plain rebar. The generated signal has 5V (peak-to-peak) amplitude, which was further amplified ten times using KRON-HITE 7500 amplifier.

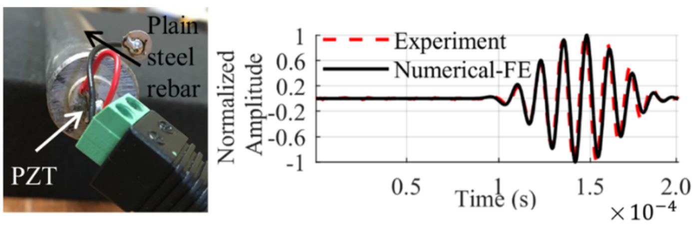

(a) (b)

Figure 10. (a) PZT installed at the end of the plain rebar (b) comparison of experimentally measured longitudinal GW signal with FE calculated signal from bare plain rebar

The signals obtained from bare rebar was normalized so that they can be compared with the data obtained from the FE simulations. The normalized signals are shown in

Figure 10(b). The experimentally measured signal has good agreement with the numerical results. In this study, the group velocity of $L(0,1)_b$ wave was calculated using the time of arrival of the absolute peak amplitude for the rebar. The excitation frequency from 50 kHz to 200 kHz were calculated for bare plain rebar and shown in the group velocity dispersion curve in Figure 11. The results of the theoretical dispersion curve from DISPERSE are also shown in the same figure. The group velocity dispersion curve for numerical, experimental and theoretical values have good agreement as shown in Figure 10.

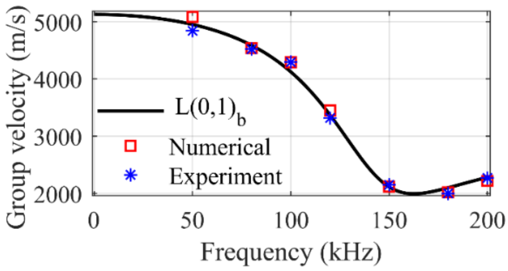

Figure 11. Group velocity dispersion curves for plain rebar

4.2 Longitudinal guided wave in reinforced concrete beam

To carry out experimental investigations, the reinforced concrete beam specimens with and without debonding were casted. The reinforced concrete beam has the same dimensions, i.e. 100mm×100mm×900mm, as the FE model shown in Figure 6. There is a section of 100mm of plain rebar extruding out from both ends. Before pouring concrete, the 900mm long plain rebar was placed at centre of 100mm×100mm cross-section formwork having the length of 700mm. In this manner, the remaining 200mm length of the plain rebar is extruded outside the formwork at both ends. The normal strength concrete was prepared with cement, sand and coarse aggregate with ratio as 1:2.5:4. The maximum size of coarse aggregate is 10mm. Two specimens were casted, in which one of them has debonding and the other is fully bonded (without debonding), to investigate the presence of second harmonic. The debonding in the specimen was created using Mylar sheet, which was wrapped around the whole surface of plain rebar at the location of 500mm from excitation location. The length of the debonding is 100mm as shown in Figure 12, which is the same as the debonding considered in the numerical model. The sheet was tightly held in place to avoid the passage of cementitious material below the Mylar.

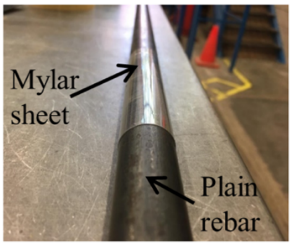

Figure 12. Debonding using Mylar sheet in plain rebar reinforced concrete specimen

The circular piezoceramic transducers are attached to the reinforced concrete beam specimens with and without debonding using epoxy glue. The experimental setup for generating and receiving of longitudinal GWs in beam specimens is shown in Figure 13. The 8-cycle sinusoidal tone burst signal with central frequency of 80kHz excited at left end of rebar had 5V (peak-to-peak) amplitude, which is amplified 50 times using KRON-

HITE amplifier to ensure the wave has large enough amplitude to generate CAN phenomenon at the debonding. Before taking measurements, it has been confirmed that there is no source of external interference at the frequencies of interest. Along with debonded sample, fully bonded sample is also tested to further confirm the nonlinearity generated due to the debonding.

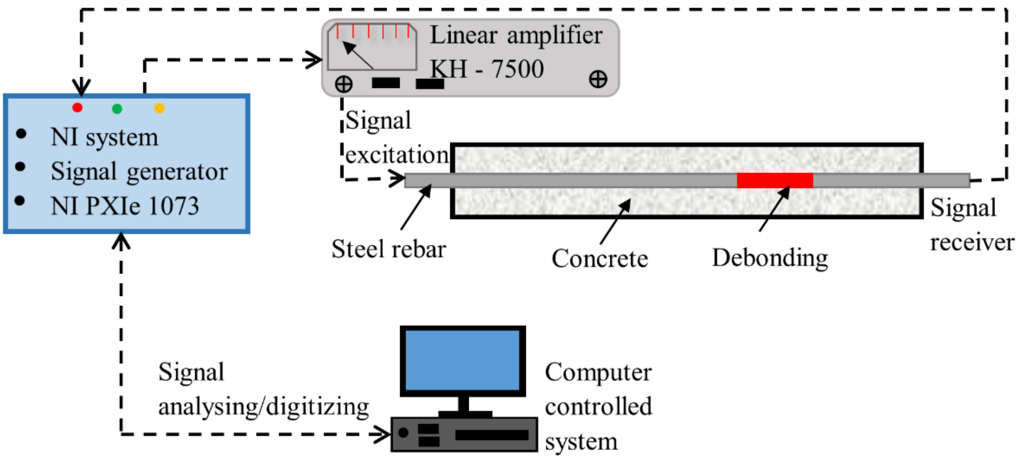

Figure 13. Experimental setup for debonding detection in reinforced concrete beam

The time domain signals for fully bonded and debonded specimens, which are experimental cases E0 and E1, were acquired in the experiment, are compared with the FE results as shown in Figures 14(a) and 14(b), respectively. The NI system has sampling rate of 6×10^7 samples per second with 14-bit depth. There is no significant difference in time domain signal between the fully bonded and debonded specimen.

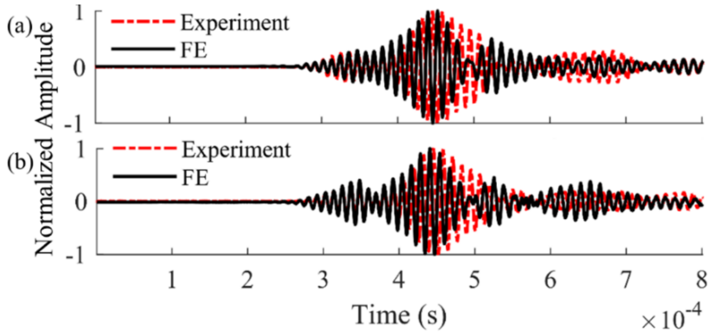

Figure 14. Experiment and FE time domain signal obtained from specimen (a) without bonding, and (b) with a debonding

The time domain signal is analysed in frequency domain using Fast Fourier Transform (FFT) with sample length of 65536 samples. The results of FFT transform are shown in Figure 15. A_1 and A_2 represents the normalized amplitude of FFT at excitation frequency (80kHz) and second harmonics (160kHz) respectively. The second harmonic can be clearly oberseved in the data obtained from debonded specimen.

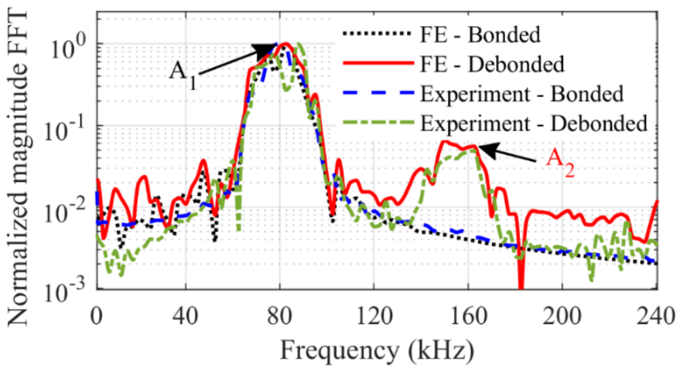

Figure 15. FFT transformed experimental and FE data obtained from the bonded and debonded specimens

For fully bonded specimens, the amplitude of frequency spectrum at the frequency of the second harmonic (160 kHz) is negligible as compared to the debonded speicmens. The observed peak at second harmonic frequency for debonded speicmen obviously indicates the presence of the debonding. For debonded sample, the nonlinear acoustic parameter β was calculated to be 0.048 and 0.054 for FE and experiment, respectively. The generation of the second harmonic is due to the CAN effect when the wave interacts at the debonding. Therefore, the presence of various wave modes in reinforced concrete can be adavantageous in a way that the amplitude of second harmonic is amplified due to multiple wave modes generating second harmonics. Therefore, the second harmonic can be used to detect debonding.

For locating debonding, the arrival time of second harmonic wave due to the debonding provides valuable information of the debonding location. The time domain signal is converted into time-frequency spectrum using Short-Time Fourier Transform (STFT). For time-frequency analysis, other methods as Wavelet Transform (WT) continuous or discrete co-exists. They can be used for good time-scale resolution as an alternative for future consideration. However, due to the uniform distribution of windowing function and segments, STFT was adopted. STFT utilizes the short duration time window τ and applies FFT on windowing function, which sweeps across the whole time domain signal t. It is mathematically described as[41]

$$S(t,\omega) = \int_{-\infty}^{+\infty} f(\tau).W(\tau - t)e^{-2\pi i\omega\tau}d\tau \qquad (4)$$

where $S(t,\omega)$ represents the time-frequency spectrum, $f(\tau)$ is the FFT function and $W(\tau - t)$ is Hann-windowed function selected on time domain signal. The time-frequency spectrum of experimentally measured and FE simulated data for fully bonded specimen are shown in Figures 16(a) and 16(b), respectively. The window length for STFT was selected to be 4096. The excitation frequency is f=80kHz and $2f$=160kHz is the second harmonic frequency. In Figure 16, the absence of the second harmonic wave at $2f$ shows that there is no debonding or contact type of damage in fully bonded specimen.

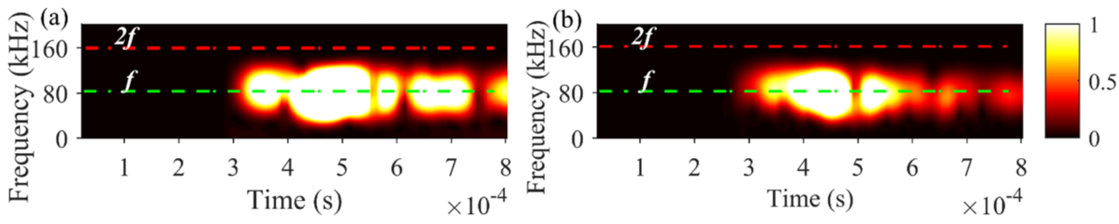

Figure 16. Time frequency spectrum of (a) experimentally measured and (b) FE simulated data for fully bonded specimen

For debonding specimen, the time-frequency analysis was also used to process the experimentally measured and FE calculated data. As observed from Figure 15, the normalized amplitude of the second harmonic is smaller than the amplitude at the excitation frequency. To clearly observe the spectrum around f and $2f$, the time-frequency spectrum is plotted at different scales for the debonded specimens. So, the second harmonic waves are detected at $2f$ for both experimentally measured and FE calculated data as shown in Figures 17(a) and 17(b), respectively.

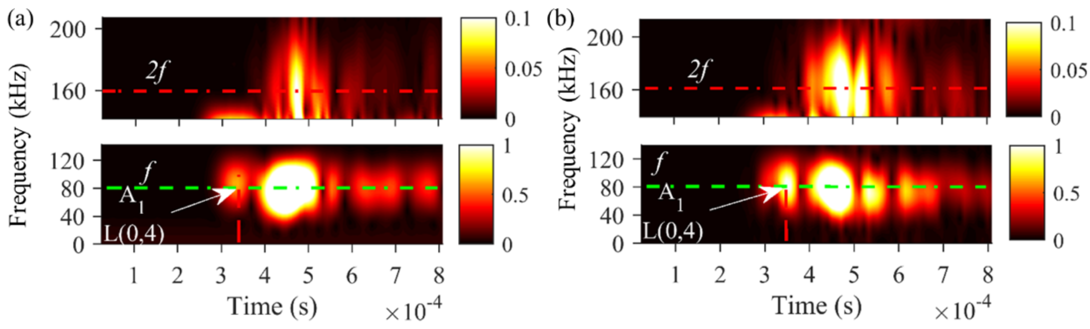

Figure 17. Time frequency spectrum of (a) experimentally measured and (b) FE simulated data for debonded specimen

From the group velocity dispersion curve of the rebar embedded in concrete, L(0,2) is the fastest and L(0,4) is the second fastest longitudinal wave mode at 80kHz. In bare rebar, only $L(0,1)_b$ is the propagating wave mode. Using the group velocity of the longitudinal wave modes for the rebar in embedded in concrete and bare rebar, the arrival time of L(0,4) is estimated to be around 0.35ms and appears to be more dominant than L(0,2) which arrives just before L(0,4) as seen in Figure 17. For time-frequency spectrum around $2f$, there are multiple wave modes propagating, which makes it complicated to identify second harmonic wave using only the information of the group velocities because the location of debonding is unknown. Therefore, the identification of multiple wave modes at second harmonic frequency for debonding location estimation is more challenging. It requires more physical insights into the presence of the wave modes propagating at f and $2f$, which is discussed using frequency wavenumber analysis in Section 5. By carefully looking into the arrival times of the corresponding wave mode at f and $2f$, the location of debonding can be determined in the case studies in Section 5.

5 Case Studies

In Section 4, the FE model has been verified that it can be used to accurately predict the wave propagation and second harmonic generation due to CAN at the debonding. This section provides a series of numerical case studies using this experimentally verified FE model to study the effect of varying debonding length on the amplitude of the second harmonic. The determination of debonding location using the second harmonic wave generated at the debonding is also demonstrated in this section.

5.1 Second harmonics for debonding damage detection

A series of numerical case studies considered in this study are summarised in Table 2, in which different lengths and locations of debondings are considered. The setup of the FE model is the same as the model shown in Figure 6. The wave is excited at location E and the wave signal is measured at the Point D.

[Table 2. Summary of debonding cases in reinforced concrete beam]

Debonding Cases	Debonding length (mm)	Midpoint of debonding from receiving location i.e. Point D (mm)
N1	100	350
N2	50	375
N3	100	550
N4	100	450
N5	150	375

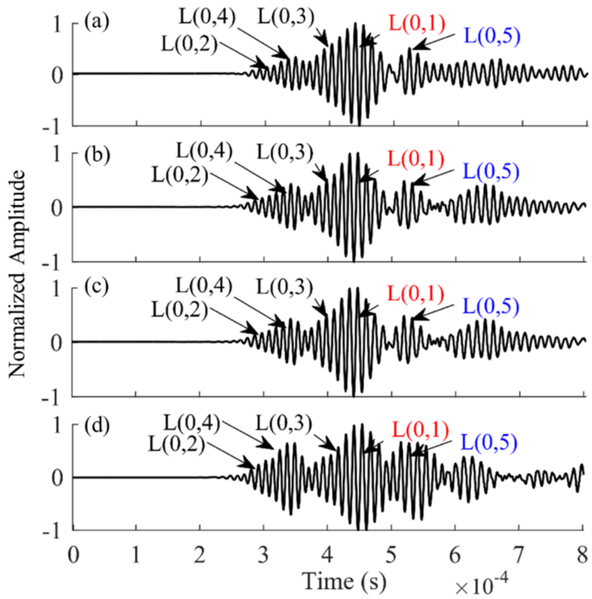

Figure 18. Time domain signals for debonding cases (a) N2, (b) N3, (c) N4, (d) N5 (results for debonding case N1 can be found in Figure 8(b))

The signals received at end of the rebar for debonded cases N2-N5 shown in Figure 18 are converted into frequency domain to identify the presence of any debonding. The FFT was performed using sample length of 65536 samples. As discussed in Section 2, the second harmonics are generated due to the CAN when the wave interact with the debonding. With complexity of various wave modes presented in time domain, it is challenging to identify any secondary wave generated in time domain signal. However, the frequency component of time domain can clearly distinguish the secondary wave generated due to the interaction between the fundamental frequency wave modes and debonding as shown in Figure 19 for debonded cases N2-N5. The variation in debonding length has impact on the amplitude of the second harmonic generation. The amplitudes of the frequency spectrum are plotted in logarithmic scale, where A_1 and A_2 represents the amplitude of fundamental and second harmonic, respectively. The second harmonic is presence in the frequency domain of the signal in all debonding cases.

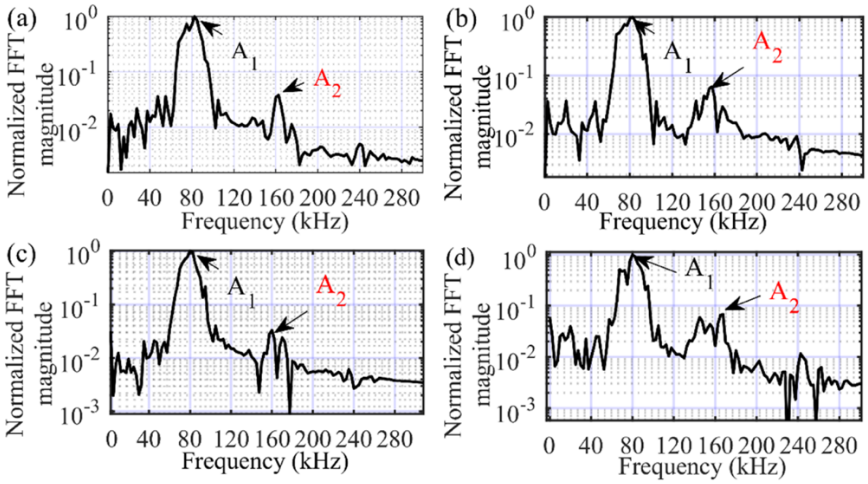

Figure 19. FFT analysis for debonded cases (a) N2, (b) N3, (c) N4, (d) N5 (results of debonding case N1 can be found in Figure 15)

The contact phenomenon generates the secondary waves and it gives valuable information about the presence of any damage without any baseline measurements. However, for locating damage, the information about wave modes at second harmonics is essential. Before developing information about wave mode content in debonded specimens, we must be aware of the presence of various wave modes for the selected reinforced concrete beam specimen as shown in Figure 6. When GW enters into reinforced concrete, $L(0,1)_b$ wave mode is converted into five longitudinal GW modes i.e. L(0,1) - L (0,5) at 80kHz as seen from dispersion curve comparison in Figure 2.

For excitation frequency f i.e. 80kHz $L(0,1)_b$ travelling at 4500m/s reduces to L(0,1) at 1780m/s for embedded rebar with higher order generated wave modes travelling at greater group velocity. At second harmonic frequency of $2f$ i.e. 160kHz, various higher order wave modes are presented. When all propagating wave modes at f interact with debonding region, the second harmonic wave modes are generated. The longitudinal GW modes increase from 5 to 10 at $2f$. The presence of wave modes at $2f$ entirely depends upon the interaction of fundamental wave modes with debonding, which is not the case with wave modes at f for which signal is excited. It is necessary to understand that upon interaction with contact surfaces, which dominant second harmonic wave modes will propagate in embedded rebar. The characteristics of wave mode content propagating after debonding is studied using frequency wavenumber analysis.

5.2 Frequency Wavenumber analysis for bare and embedded rebar in concrete

The wave data extracted over space for known time provides valuable information about presence of wave modes propagating in space[42]. The two-dimensional Fast Fourier transform (2D-FFT) is implemented on time-space wavefield to acquire frequency wavenumber representation. In the time-space wave data analysis, frequency is the representation of time and wavenumber is the representation of space for the propagating wave. The longitudinal GW data over time-space can be transformed into frequency wavenumber representation and it is mathematically defined as

$$U(f,k) = \int_{-\infty}^{+\infty} \int_{-\infty}^{+\infty} u(t,x) e^{-j(2\pi f t - kx)} dt dx \qquad (6)$$

where $U(f,k)$ is frequency wavenumber representation obtained using 2D-FFT of time-space data. u represents displacement of propagating longitudinal wave. t and x is time and distance data, respectively. The presence of dominating wave mode content can be reflected in time-frequency spectrum.

Frequency wavenumber spectrum analysis is carried out for a distance of 200mm in the rebar embedded in concrete, which is the region between Point B and C as shown in Figure 6(a) and the region is located after the debonding. The longitudinal displacement is obtained for 0.8ms at every 2mm in this region. In Figure 20(a), the frequency wavenumber spectrum for various wave modes propagating from frequency 0 to 200kHz is plotted together with the results obtained from DISPERSE. The spectrum clearly shows the presence of fundamental frequency wave modes at 80kHz and second harmonic wave modes at 160kHz. The spectrum for rebar embedded in concrete shows the presence of L(0,1) – L(0,5) GW modes at f=80kHz with L(0,4) having the most dominant wave mode content. At $2f$=160kHz, L(0,6) – L(0,10) GW modes are generated, which have small amplitude in the spectrum, and hence, the L(0,4) is the dominant wave mode at $2f$. Therefore, this make it easy to identify its time of arrival for L(0,4). The value of the group velocity of L(0,4) at $2f$ is less than that at f. This means that L(0,4) GW mode at $2f$ arrives after L(0,4) GW mode at f in the time-frequency spectrum.

After debonding region, all GW modes for the rebar embedded in concrete at f and $2f$ upon entering into bare rebar travel with group velocity of $L(0,1)_b$ at f and $2f$, respectively. This is confirmed by performing the frequency wavenumber analysis from the data obtained in the bare rebar region C-D as shown in Figure 6(a). Similarly, the time-space data is acquired for 1ms at every 2mm in this 100mm long section of the extruding rebar. The frequency wavenumber spectrum for bare rebar has only one propagating GW mode $L(0,1)_b$ as shown in Figure 20(b) at f and $2f$. The information about GW mode content in embedded and bare rebar regions is essential for choosing dominant wave mode content in debonding location estimation using time-frequency analysis.

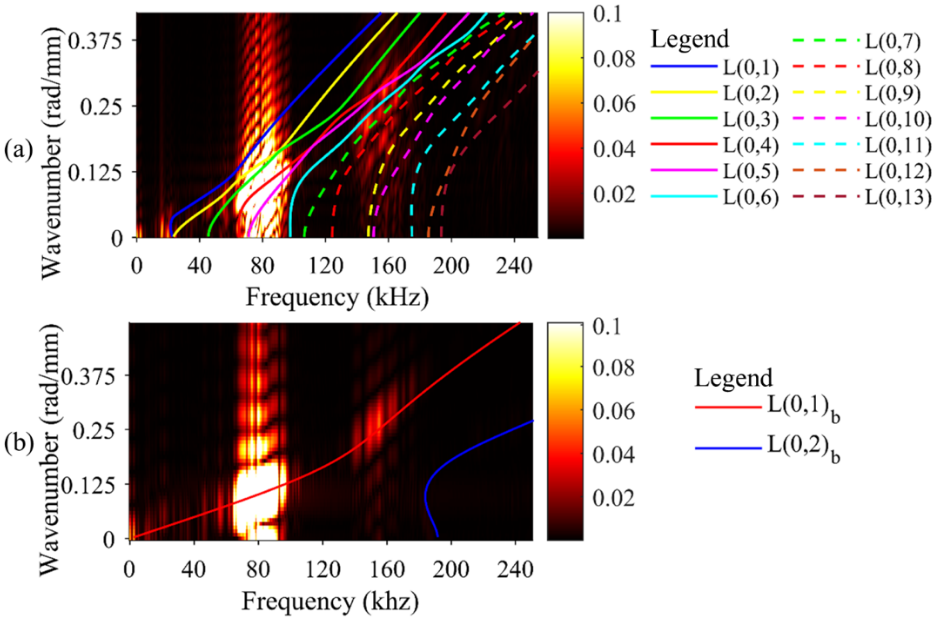

Figure 20. Frequency-wavenumber spectrum for propagating longitudinal wave (a) after debonding for rebar embedded in concrete, and (b) extruding bare rebar

5.3 Time delay in second harmonic generation for dominant wave mode

The fundamental GW modes propagating in embedded rebar generates secondary wave modes upon interaction with debonding damage. As shown in Figure 2, L(0,2) is the fastest wave mode for embedded rebar at f and is followed by L(0,4), L(0,3), L(0,1,) and L(0,5) in order. However, L(0,4) has proven to be the more dominant as compared to L(0,2) frequency wavenumber analysis. Upon interaction with debonding, the L(0,4) wave mode at f generates second harmonic L(0,4) wave mode, which is also the most dominant wave mode at $2f$ as proven from frequency wavenumber analysis. To accurately determine the location of debonding, the time delay in generation of second harmonic needs to be taken into account.

For verifying the presence of time delay, time-frequency spectrum analysis is carried out using STFT for the data obtained at Point A as shown in Figure 6(a). The time-frequency spectrum is analysed at $2f$. The arrival time of L(0,4) wave mode at f depends upon the group velocity of $L(0,1)_b$ wave mode at f in bare rebar (region E-F in Figure 6) and L(0,4) wave mode at f in embedded rebar (region F-A in Figure 6). The arrival time is estimated to be 2.36×10^{-4}s as shown by solid line in Figure 21. From results in frequency-wavenumber analysis, the dominant L(0,4) second harmonic wave mode will be propagating after debonding. The dominant wave mode content at $2f$ shall appear at the arrival time of L(0,4) at f. However, the time-frequency spectrum shows a time delay in the arrival time of L(0,4) second harmonic wave mode. The time delay is 6×10^{-5}s as shown in Figure 21, which is calculated by measuring the delayed arrival time at peak amplitude of $2f$. The delay is due to the time for generating the second harmonic wave when the incident wave interacts with the debonding.

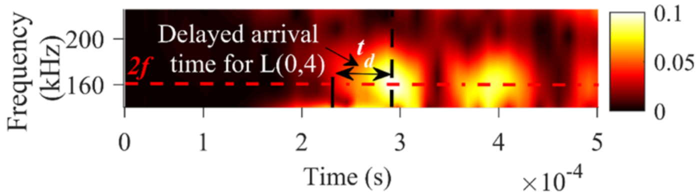

Figure 21. Time-frequency spectrum of the data obtained at Point A from the rebar embedded in concrete

The calculated time delay t_d is used to estimate the location of debonding. For the embedded rebar, the group velocity L(0,4) wave mode at f is around 2700m/s while for L(0,5) wave mode at $2f$ is around 1900m/s, which indicates that the dominant second harmonic L(0,4) wave mode arrive after L(0,4) wave mode at f in time-frequency spectrum.

5.4 Debonding location estimation

The analysis in Section 5.3 has provided valuable information on the dominant wave mode content at $2f$ and time-delay in the generation of second harmonic wave mode. For estimating the location of debonding, the arrival times of L(0,4) wave mode at f and $2f$ are utilized. Time-frequency spectrum of debonding cases N2-N5, which are individually analysed at different scales for distinguishing the spectrum at f and $2f$ as 0-1 and 0-0.1, are shown in Figures 22(a)-22(d). The amplitudes at the f and $2f$ of the time-frequency spectrum are shown in Figure 23 and the amplitudes are normalized. The arrival times of L(0,4) wave mode at f and $2f$ are estimated by the respective peak amplitudes. For the data at the excitation frequency *f*=80kHz, although the magnitudes of the peaks appear to be more dominant than the first peak, which is the arrival time of L(0,4) wave mode, it is entirely due to the presence of L(0,3), L(0,1) and L(0,5) wave modes enlarging the amplitudes of the waves arrived after L(0,4).

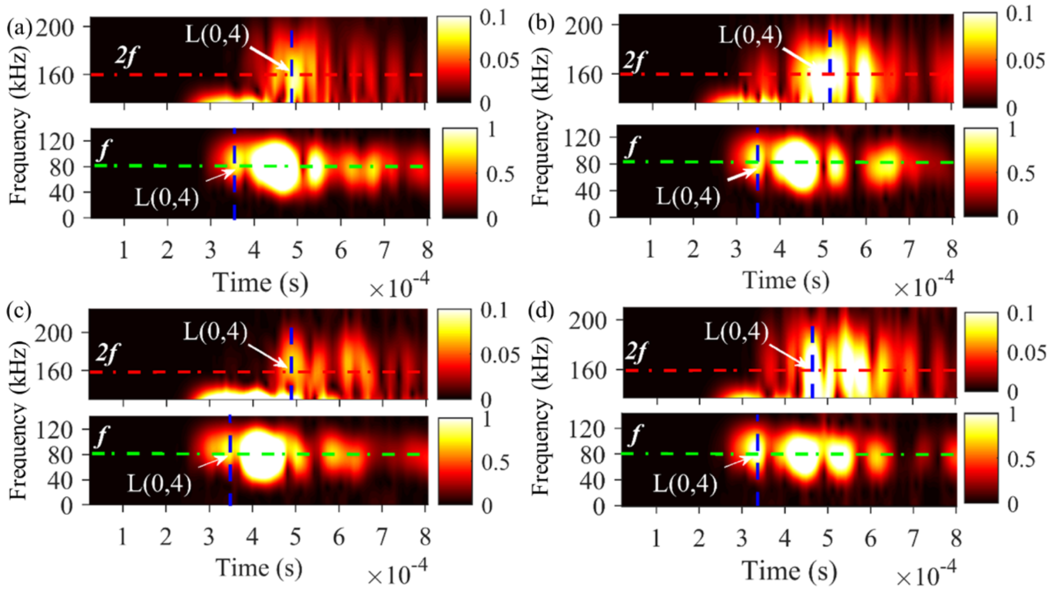

Figure 22. Time-frequency spectrum for debonding cases (a) N2, (b) N3, (c) N4, (d) N5 (results of debonding case N1 can be found in Figure 17(b))

At $2f$, the peak amplitude lies at L(0,4) wave mode and its time of arrival is estimated using peak amplitude of time frequency spectrums and their respective FT plots. The arrival time of L(0,4) at f and $2f$ is selected at the center of L(0,4) wave mode time frequency spectrum. The difference in arrival time of L(0,4) at f and $2f$ gives Δt as defined in section 2. Using equation 3 derived in section 2.3 and utilizing the time delay t_d, the debonding location estimated for debonding cases N2-N5 are shown in Table 3.

[Table 3. Debonding location estimation using second harmonic wave]

Debonding Cases	Wave Frequency (kHz)	Arrival time (s) of L(0,4) at Point D, (receiving location)	Estimated debonding location from Point D (mm)	Actual debonding location from Point D (mm) (Start – End location of debonding)
N1	160	$4.78\times\ 10^{-4}$	351	300-400
	80	$3.50\times\ 10^{-4}$		
N2	160	$4.90\times\ 10^{-4}$	371	350-400
	80	$3.60\times\ 10^{-4}$		
N3	160	$5.10\times\ 10^{-4}$	560	500-600
	80	$3.50\times\ 10^{-4}$		
N4	160	$4.92\times\ 10^{-4}$	448	400-500
	80	$3.50\times\ 10^{-4}$		
N5	160	$4.70\times\ 10^{-4}$	371	250-400
	80	$3.40\times\ 10^{-4}$		

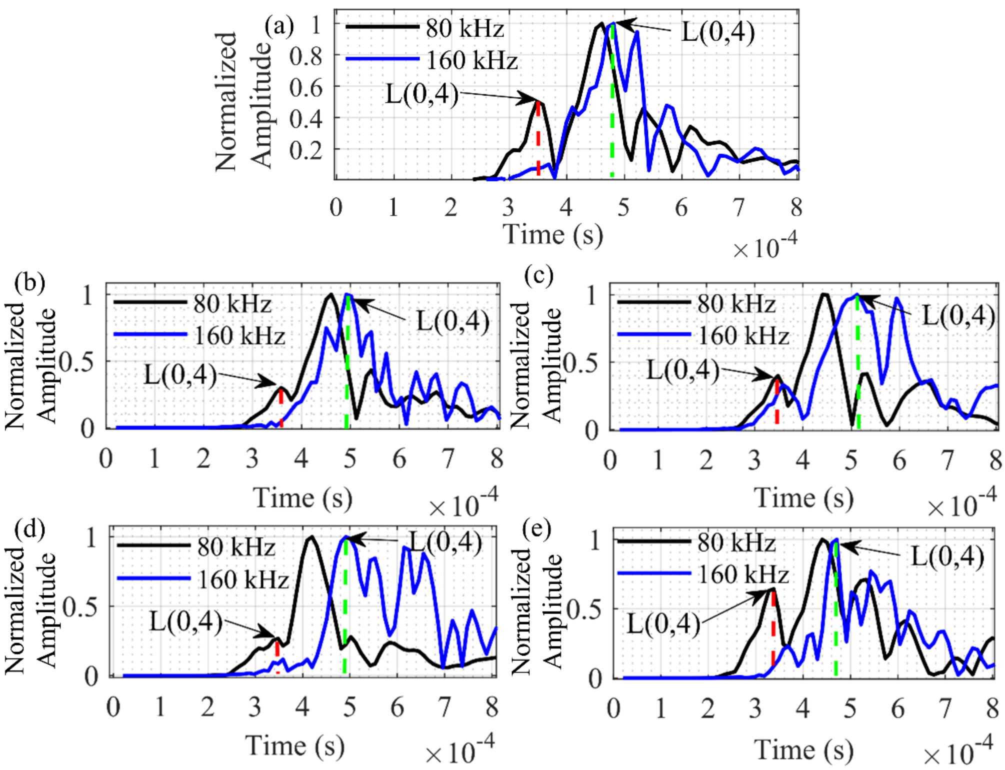

Figure 23. Amplitudes at f and 2f of the frequency-time spectrum for debonding cases (a) N1, (b) N2, (c) N3, (d) N4 and (e) N5

The locations of debondings for all debonded cases are accurately estimated and lie within the debonding region as shown in Table 3. For varying debonding lengths, the estimation of location is around the center of debonding. For experimental case E1 with debonding, the arrival time of L(0,4) wave mode at f and $2f$ is estimated as 3.52×10^{-4}s and 4.80×10^{-4}s, respectively, as shown in Figure 17(a). The estimated debonding location is 356mm from Point D, which is within the actual debonding start-end location, 300mm–400mm, from Point D. Therefore, the nonlinear features of longitudinal guided waves can be used to accurately determine the location of debonding in rebar reinforced concrete.

5.5 Relationship between nonlinear acoustic parameter and debonding length

The presence of second harmonic is sensitive to the size of debonding. The amplitude of second harmonic generated varies with the length of debonding as observed in FFT analysis. The nonlinear acoustic parameter β as defined in section 2 is used to understand the relation for varying debonding sizes with generated second harmonic.

Three debonded cases N1, N2 and N5 with varying debonding lengths at fixed location are selected. The peak normalized amplitude around excitation frequency f i.e. A_1 and normalized amplitude around second harmonic frequency $2f$, i.e. A_2 is used to calculate β, which is plotted against debonding length for selected cases as shown in Figure 24. With increasing debonding length, the nonlinear acoustic parameter β also increases. By looking at Figure 24, the relation between β and debonding length appear to be nonlinear and increasing. Therefore, the amplitude of second harmonic generated is larger for greater debonding lengths.

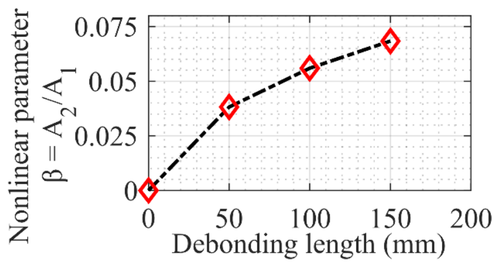

Figure 24. Relative nonlinear acoustic parameter for different debonding lengths

6 Conclusion

In this study, the nonlinear feature of longitudinal GW has been proposed to detect and locate debonding in reinforced concrete beam. The nonlinear feature, second harmonic, is generated due to CAN effect at debonding. Both numerical and experimental studies have been carried out in this study. The FE model of reinforced concrete beam with and without debonding has been developed to predict the presence of second harmonic due to CAN at debonding. The FE model has also been experimentally verified. There is good agreement between FE simulated and experimentally measured second harmonics. The numerical and experimental studies have provided physical insights into the second harmonic generation at debonding.

It has been found that the time delay in generating the second harmonic wave when the incident wave interacts with debonding needs to be considered for estimating the debonding location. Due to the presence of multiple longitudinal GW modes in reinforced concrete beam at excitation frequency and second harmonics frequency, frequency-wavenumber analysis has been performed to understand various propagating wave modes.

Five different debonded cases with varying debonding size and location have been studied. Time-frequency spectrum has been used to analyse signals for location estimation. The results have shown that second harmonic can be used to accurately detect the existence of debonding and the debonding location. Finally, the study has also shown that there is a relationship between the relative nonlinear acoustic parameter to the debonding size and it can be used as an indicator of the debonding size.

7 Acknowledgement

This work was supported by Australian Research Training Program and Australian Research Council through DP200102300. The support is greatly appreciated.

8 References

1. Zhao, Y.a., *Steel corrosion-induced concrete cracking*, ed. W.a. Jin. 2016: Elsevier.
2. Sriramadasu, R.C., S. Banerjee, and Y. Lu, *Detection and assessment of pitting corrosion in rebars using scattering of ultrasonic guided waves.* Ndt & E International, 2019. **101**: p. 53-61.
3. Salençon, J., W. Ostachowicz, and J.A. Güemes, *New Trends in Structural Health Monitoring*. Vol. 542. 2012, Vienna: Vienna: Springer.
4. Büyüköztürk, O.a., *Nondestructive Testing of Materials and Structures*, ed. M.A.a. Taşdemir, et al. 2013: Springer Netherlands : Imprint: Springer.
5. Kim, G., et al., *In situ nonlinear ultrasonic technique for monitoring microcracking in concrete subjected to creep and cyclic loading.* Ultrasonics, 2018. **88**: p. 64-71.

6. Chen, J., C. Yang, and Q. Guo, *Evaluation of surface cracks of bending concrete using a fully non-contact air-coupled nonlinear ultrasonic technique.* Materials and Structures, 2018. **51**(4): p. 1-9.
7. Mustapha, S., et al., *Damage detection in rebar-reinforced concrete beams based on time reversal of guided waves.* Structural Health Monitoring-an International Journal, 2014. **13**(4): p. 347-358.
8. Lu, Y., et al., *Guided waves for damage detection in rebar-reinforced concrete beams.* Construction and Building Materials, 2013. **47**: p. 370-378.
9. Sabet Divsholi, B. and Y. Yang, *Combined embedded and surface-bonded piezoelectric transducers for monitoring of concrete structures.* NDT & E International, 2014. **65**: p. 28-34.
10. Zhu, X.Q., H. Hao, and K.Q. Fan, *Detection of delamination between steel bars and concrete using embedded piezoelectric actuators/sensors.* Journal of Civil Structural Health Monitoring, 2013. **3**(2): p. 105-115.
11. Wu, F. and F.K. Chang, *Debond detection using embedded piezoelectric elements in reinforced concrete structures - Part I: Experiment.* Structural Health Monitoring-an International Journal, 2006. **5**(1): p. 5-15.
12. Wu, F. and F.K. Chang, *Debond detection using embedded piezoelectric elements for reinforced concrete structures - Part II: Analysis and algorithm.* Structural Health Monitoring-an International Journal, 2006. **5**(1): p. 17-28.
13. Ou, G., et al., *Identifi cation of de-bonding between steel bars and concrete using wavelet techniques: Comparative study.* Australian Journal of Structural Engineering, 2013. **14**(1): p. 43-56.
14. Mohseni, H. and C.-T. Ng, *Rayleigh wave propagation and scattering characteristics at debondings in fibre-reinforced polymer-retrofitted concrete structures.* Structural Health Monitoring, 2019. **18**(1): p. 303-317.
15. Sriramadasu, R.C., Y. Lu, and S. Banerjee, *Identification of incipient pitting corrosion in reinforced concrete structures using guided waves and piezoelectric wafer transducers.* Structural Health Monitoring-an International Journal, 2019. **18**(1): p. 164-171.
16. Sharma, A., et al., *Investigation of deterioration in corroding reinforced concrete beams using active and passive techniques.* Construction and Building Materials, 2018. **161**: p. 555-569.
17. Sharma, S. and A. Mukherjee, *Longitudinal Guided Waves for Monitoring Chloride Corrosion in Reinforcing Bars in Concrete.* Structural Health Monitoring-an International Journal, 2010. **9**(6): p. 555-567.
18. Majhi, S., et al., *Corrosion detection in steel bar: A time-frequency approach.* Ndt & E International, 2019. **107**.

19. Reis, H., et al., *Estimation of corrosion damage in steel reinforced mortar using waveguides.* Nondestructive Evaluation and Health Monitoring of Aerospace Materials, Composites, and Civil Infrastructure Iv, 2005. **5767**: p. 98-107.
20. Zima, B. and R. Kędra, *Reference-free determination of debonding length in reinforced concrete beams using guided wave propagation.* Construction and Building Materials, 2019. **207**: p. 12.
21. Beata, Z. and K. Rafał, *Debonding Size Estimation in Reinforced Concrete Beams Using Guided Wave-Based Method.* Sensors, 2020. **20**(2): p. 389.
22. Soleimanpour, R. and C.T. Ng, *Locating delaminations in laminated composite beams using nonlinear guided waves.* Engineering Structures, 2017. **131**: p. 207-219.
23. Mohseni, H. and C.T. Ng, *Higher harmonic generation of rayleigh wave at debondings in frp-retrofitted concrete structures.* Smart Materials and Structures, 2018. **27**(10): p. 105038.
24. Chen, J., C.L. Yang, and Q.Q. Guo, *Evaluation of surface cracks of bending concrete using a fully non-contact air-coupled nonlinear ultrasonic technique.* Materials and Structures, 2018. **51**(4).
25. Hikata, A., B.B. Chick, and C. Elbaum, *Dislocation Contribution to the Second Harmonic Generation of Ultrasonic Waves.* Journal of Applied Physics, 1965. **36**(1): p. 229-236.
26. Ding, X., et al., *Experimental and Numerical Study of Nonlinear Lamb Waves of a Low-Frequency S 0 Mode in Plates with Quadratic Nonlinearity.* Materials, 2018. **11**(11).
27. Li, W. and Y. Cho, *Thermal Fatigue Damage Assessment in an Isotropic Pipe Using Nonlinear Ultrasonic Guided Waves.* Experimental Mechanics, 2014. **54**(8): p. 1309-1318.
28. Thiele, S., et al., *Air-coupled detection of nonlinear Rayleigh surface waves to assess material nonlinearity.* Ultrasonics, 2014. **54**(6): p. 1470-1475.
29. Bermes, C., et al., *Nonlinear Lamb waves for the detection of material nonlinearity.* Mechanical Systems and Signal Processing, 2008. **22**(3): p. 638-646.
30. Wang, K., et al., *Analytical insight into "breathing" crack-induced acoustic nonlinearity with an application to quantitative evaluation of contact cracks.* Ultrasonics, 2018. **88**: p. 157-167.
31. Solodov, I.Y., N. Krohn, and G. Busse, *CAN: an example of nonclassical acoustic nonlinearity in solids.* Ultrasonics, 2002. **40**(1): p. 621-625.
32. Broda, D., et al., *Generation of higher harmonics in longitudinal vibration of beams with breathing cracks.* Journal of Sound and Vibration, 2016. **381**: p. 206-219.

33. Wang, K., et al., *Nonlinear aspects of "breathing" crack-disturbed plate waves: 3-D analytical modeling with experimental validation.* International Journal of Mechanical Sciences, 2019. **159**: p. 140-150.
34. Klepka, A., et al., *Nonlinear acoustics for fatigue crack detection – experimental investigations of vibro-acoustic wave modulations.* Structural health monitoring, 2012. **11**(2): p. 197-211.
35. Guan, R.Q., et al., *Fatigue crack detection in pipes with multiple mode nonlinear guided waves.* Structural Health Monitoring-an International Journal, 2019. **18**(1): p. 180-192.
36. Radecki, R., et al., *Modelling nonlinearity of guided ultrasonic waves in fatigued materials using a nonlinear local interaction simulation approach and a spring model.* Ultrasonics, 2018. **84**: p. 272-289.
37. Pavlakovic, B., et al., *Disperse: A general purpose program for creating dispersion curves.* Review of Progress in Quantitative Nondestructive Evaluation, Vols 16a and 16b, 1997. **16**: p. 185-192.
38. Shah, A.A., Y. Ribakov, and C. Zhang, *Efficiency and sensitivity of linear and non-linear ultrasonics to identifying micro and macro-scale defects in concrete.* Materials & Design, 2013. **50**: p. 905-916.
39. *Local Bond-Stress to Slip Relationships for Hot Rolled Deformed Bars and Mild Steel Plain Bars.* ACI Journal Proceedings, 1979. **76**(3).
40. Wan, X., et al., *Numerical Simulation of Nonlinear Lamb Waves Used in a Thin Plate for Detecting Buried Micro-Cracks.* Sensors, 2014. **14**(5): p. 8528-8546.
41. Sharma, G.K., et al., *Short time Fourier transform analysis for understanding frequency dependent attenuation in austenitic stainless steel.* NDT and E International, 2013. **53**: p. 1-7.
42. Michaels, T.E., J.E. Michaels, and M. Ruzzene, *Frequency–wavenumber domain analysis of guided wavefields.* Ultrasonics, 2011. **51**(4): p. 452-466.